Physics of the Earth and Planetary Interiors 180 (2010) 179–188

Contents lists available at ScienceDirect

Physics of the Earth and Planetary Interiors

journal homepage: www.elsevier.com/locate/pepi

# Tetrahedral occupancy of ferric iron in (Mg,Fe)O: Implications for point defects in the Earth's lower mantle

Kazuhiko Otsuka[a,*], Catherine A. McCammon[b], Shun-ichiro Karato[a]

[a] Yale University, Department of Geology and Geophysics, 210 Whitney Avenue, New Haven, CT, 06511, USA
[b] Bayerisches Geoinstitut, Universität Bayreuth, D-95440, Bayreuth, Germany

ARTICLE INFO

*Article history:*
Received 3 June 2009
Received in revised form
16 September 2009
Accepted 16 October 2009

Guest Editors
Kei Hirose
Thorne Lay
David Yuen

Editor
G. Helffrich

*Keywords:*
Ferric iron
Lower mantle
(Mg,Fe)O
Mössbauer spectroscopy
Point defects
Transport properties

ABSTRACT

We investigated the concentration and site occupation of ferric iron ($Fe^{3+}$) in (Mg,Fe)O to understand the influence of point defects on transport properties such as atomic diffusion, electrical conductivity and viscosity. We conducted Mössbauer spectroscopy of $(Mg_{0.8}Fe_{0.2})O$ single crystals synthesized at temperatures from 1673 to 2273 K and pressures from 5 to 15 GPa with Re–$ReO_2$ and Mo–$MoO_2$ oxygen fugacity buffers. The isomer shift of the Mössbauer spectra suggests that $Fe^{3+}$ occupies mostly the tetrahedral site at reduced conditions and both the octahedral and tetrahedral sites at oxidized conditions. We formulate a thermodynamic model of point defect dissolution in (Mg,Fe)O which suggests that unassociated tetrahedral $Fe^{3+}$ is more stable than unassociated octahedral $Fe^{3+}$ at high-pressure and low oxygen fugacity due to the effect of configurational entropy. The pressure dependence of $Fe^{3+}$ concentration indicates a change in the dominant site occupancy of $Fe^{3+}$: (1) $Fe^{3+}$ in the tetrahedral site, (2) $Fe^{3+}$ in the octahedral site, and (3) defect clusters of $Fe^{3+}$ and cation vacancy, in the order of increasing oxygen fugacity and decreasing pressure. This is in reasonable agreement with previously reported experiments on $Fe^{3+}$ concentration, Mg–Fe interdiffusivity and electrical conductivity. We consider it plausible that (Mg,Fe)O accommodates $Fe^{3+}$ in the tetrahedral site down to the lower mantle. Based on our results and available experimental data, we discuss the solubility competition between $Fe^{3+}$ and protons ($H^+$), and its implications for transport properties in the lower mantle.



## 1. Introduction

The knowledge of transport properties such as atomic diffusion, viscosity and electrical conductivity in lower mantle phases is critical for understanding the dynamics of the lower mantle and interpreting geophysical observations such as electrical conductivity (e.g., Kelbert et al., 2009) or seismic wave attenuation (e.g., Lawrence and Wysession, 2006). The ferropericlase–magnesiowüstite solid solution (Mg,Fe)O, is considered to be the second most abundant phase in the lower mantle, comprising ~20% in the pyrolite model (e.g., Hirose, 2002). (Mg,Fe)O has noticeably higher atomic diffusivity (Holzapfel et al., 2003; Van Orman et al., 2009; Yamazaki and Irifune, 2003), lower viscosity (Poirier et al., 1986; Yamazaki and Karato, 2001), and higher electrical conductivity (Dobson et al., 1997; Ohta et al., 2007; Wood and Nell, 1991; Xu and McCammon, 2002) than magnesium silicate perovskite, the most abundant phase in the lower mantle. Therefore, these transport properties of the lower mantle are likely controlled largely by those of (Mg,Fe)O. Transport properties are highly sensitive to the presence of point defects. Consequently, it is important to characterize the concentration and site occupation of point defects under a wide range of experimental conditions in order to understand the mechanisms that control transport processes and to enable the projection of lower mantle properties through extrapolation of laboratory measurements.

Various investigations have been conducted on point defects in (Mg,Fe)O (e.g., Hirsch and Shankland, 1991). (Mg,Fe)O crystallizes in the B1 (rock salt) structure where the cations occupy a face-centered cubic sublattice. At atmospheric pressure, trivalent iron (ferric iron or $Fe^{3+}$) is the most abundant positively charged point defect in (Mg,Fe)O, which is charge balanced by negatively charged cation vacancies (e.g., Hazen and Jeanloz, 1984). Based on neutron scattering, Mössbauer and X-ray emission spectroscopy, it has been recognized that $Fe^{3+}$ occupies not only octahedrally coordinated cation sites but also tetrahedrally coordinated interstitial sites, which are normally vacant in the ideal structure (e.g., Hazen and Jeanloz, 1984; Hilbrandt and Martin, 1998; Jacobsen et al., 2002; Waychunas, 1983). Tetrahedral $Fe^{3+}$ is observed in (Mg,Fe)O with sufficiently high ratio of $Fe^{3+}/[Fe^{2+}+Fe^{3+}]$ ($Fe^{3+}/\sum Fe$) at oxidized conditions near the phase boundary with magnesioferrite

* Corresponding author. Tel.: +1 203 432 5791; fax: +1 203 432 3134.
*E-mail address:* kazuhiko.otsuka@yale.edu (K. Otsuka).

0031-9201/$ – see front matter © 2009 Elsevier B.V. All rights reserved.
doi:10.1016/j.pepi.2009.10.005

($MgFe_2O_4$), which is likely different from the more reduced conditions inferred for the lower mantle (e.g., Frost and McCammon, 2008). Thus, previous studies on transport properties commonly assumed that $Fe^{3+}$ resides only in the octahedral site of (Mg,Fe)O in the lower mantle (e.g., Yamazaki and Irifune, 2003). No detailed studies, however, have been conducted considering the site occupation of $Fe^{3+}$ at reduced conditions and high pressures.

The $Fe^{3+}/\sum Fe$ ratio at ambient pressure varies with temperature, oxygen fugacity, and Mg/Fe ratio (e.g., Hilbrandt and Martin, 1998; Katsura and Kimura, 1965; Speidel, 1967). The influence of pressure was explored by McCammon et al. (1998), who concluded that $Fe^{3+}$ solubility in (Mg,Fe)O decreases with pressure based on Mössbauer spectroscopy analysis of their multi-anvil and diamond anvil cell experiments. Follow-up experiments using Mössbauer spectroscopy or electron energy-loss near-edge structure (ELNES) spectroscopy reported $Fe^{3+}/\sum Fe$ ratios of 1–19% in (Mg,Fe)O with Mg numbers ($Mg\# = Mg/[Mg+Fe] \times 100$ in an atomic ratio) of 80–93 at 1473–2123 K and 25–26 GPa under oxidized conditions imposed by Re-$ReO_2$ (Bolfan-Casanova et al., 2002; Frost and Langenhorst, 2002; McCammon et al., 2004). Bolfan-Casanova et al. (2002) also suggested that the dominant positively charged defects may change from $Fe^{3+}$ to protons ($H^+$) at high-pressure since $H^+$ solubility increases with pressure under water-saturated conditions. The behavior of transport properties may thus change with pressure from mechanisms sensitive to $Fe^{3+}$ content (or oxygen fugacity) to those sensitive to $H^+$ content (or water fugacity). Therefore, it is important to explore conditions of the solubility crossover between $Fe^{3+}$ and $H^+$ as a guide to understand the nature of such a threshold of material behavior. The previous high-pressure experiments were, however, conducted under a limited range conditions, mostly at high oxygen fugacity or a single temperature. It is not yet clear whether or not such a solubility crossover occurs in the lower mantle.

In this study, therefore, we investigate the equilibrium concentration and site occupation of $Fe^{3+}$ in (Mg,Fe)O based on Mössbauer spectroscopy analysis. We extend experiments to a wider range of temperature and oxygen fugacity relevant to the lower mantle and present a thermodynamic model to examine the influence of thermochemical states based on our new experimental results combined with those of early studies. Finally we discuss implications of these results for transport properties in the lower mantle.

## 2. Experimental methods

### 2.1. Starting material

The starting materials for the high-pressure experiments were synthetic (Mg,Fe)O single crystals. The (Mg,Fe)O crystals were prepared by interdiffusion between a MgO single crystal with a thickness of 0.5 mm and reagent grade oxides of periclase (MgO) and hematite ($Fe_2O_3$) powder in the appropriate ratio for Mg#80. The nominal impurity content of the MgO single crystal was 40 ppm Ca, 15 ppm Al, 50 ppm Fe, 10 ppm Cr, 5 ppm B, and 10 ppm C according to the supplier (SPI supply). The MgO single crystal plate embedded in oxides was annealed in a vertical tube furnace operated at 1873 K for 200 h in total under an oxygen fugacity of 1 Pa (1.5 log–bar units below the phase boundary between magnetite ($Fe_3O_4$) and wüstite ($Fe_{1-\delta}O$)) controlled by a mixture of CO and $CO_2$ gas. Annealing experiments were quenched by shutting down the power supply. We did not measure $Fe^{3+}$ concentrations of recovered samples but we estimate them based on literature data to be ~3% ($Fe^{3+}/O$). The gas mixing ratio and oxygen fugacity relation was calibrated at 1473 K using the phase boundaries between magnetite and wüstite and between metallic nickel (Ni) and bunsenite (NiO). The synthesized single crystals were analyzed by a field-emission-gun scanning electron microprobe (XL30 ESEM-FEG) and an electron probe micro-analyzer with a wavelength dispersive system (JXA-8600). Chemical analysis was performed using an accelerating voltage of 10 kV and a beam current of 10 nA. The chemical composition of recovered samples ranged between 79 and 84 in Mg# and varied less than 1% over the sample size of high-pressure experiments (0.8 mm). Hereafter, we refer to this composition as $Mg_{0.8}Fe_{0.2}O$. There was no detectable contamination of elements other than Fe, Mg and O.

### 2.2. Generation of high-pressure and high-temperature

High-pressure annealing experiments were performed with a 1000-ton Kawai-type multi-anvil apparatus installed at Yale University with the conventional 18-11 or 14-8 assembly. The confining pressure was exerted on the cell assembly by eight tungsten carbide cubes with an edge length of 26 mm and a corner truncation of either 11 or 8 mm. The pressure media consist of a semi-sintered $Cr_2O_3$-doped MgO octahedron with an edge length of 18 or 14 mm, a graphite or $LaCrO_3$ stepped cylindrical furnace, and a $ZrO_2$ sleeve enveloping the furnace as a thermal insulation. Temperature was monitored with a $W_5Re$–$W_{26}Re$ thermocouple with a thermocouple junction placed in direct contact with one end of the sample capsule. The sample charge was electrically insulated from the furnace by an MgO sleeve. The uncertainty of temperature and pressure was estimated as ±80 K and ±0.5 GPa, respectively, based on previous experiments (Nishihara et al., 2006).

The oxygen fugacity in the samples was controlled by two different metal-oxide buffers: Re–$ReO_2$ for an oxidized condition and Mo–$MoO_2$ for a reduced condition as schematically shown in Fig. 1. The synthetic $Mg_{0.8}Fe_{0.2}O$ single crystals with an approximate edge length of 0.8 mm with thickness of 0.5 mm were placed in the inner Re and Mo capsules, where corresponding oxides (either $ReO_2$ or $MoO_2$ powder, respectively) were added together with $Mg_{0.8}Fe_{0.2}O$ powder. The $Mg_{0.8}Fe_{0.2}O$ powder was prepared from a mixture of MgO and $Fe_2O_3$ which was annealed for 14 h at 1473 K at an oxygen fugacity of $10^{-5}$ Pa (1 log–bar unit below the phase boundary between magnetite and wüstite). Each of the Re and Mo capsules was loaded into an AuPd or Pt outer tube capsule of 0.2 mm wall thickness. The outer tube capsule was welded to minimize the water input from the surrounding environment. Thus, two different oxygen fugacity environments were imposed on two different samples in a single high-pressure experiment.

### 2.3. Mössbauer spectroscopy

Mössbauer spectra of $^{57}Fe$ in $Mg_{0.8}Fe_{0.2}O$ were recorded at room temperature and pressure in transmission geometry at Bayerisches

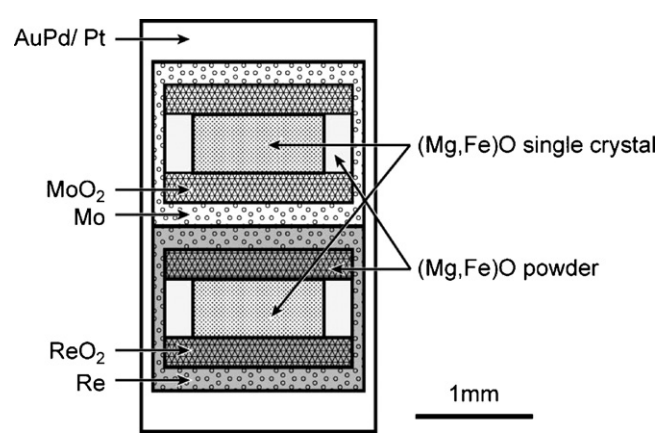


**Fig. 1.** Schematic diagram of the capsule assembly for the 18/11 cell.

**Table 1**
Conditions of high-pressure annealing experiments and results.

| Run no. | Pressure [GPa] | Temperature [K] | Duration [min] | Capsule | Mo–$MoO_2$ buffer | | Re–$ReO_2$ buffer | |
|---|---|---|---|---|---|---|---|---|
| | | | | | Oxide | Mg# | Oxide | Mg# |
| K731 | 5 | 1673 | 120 | AuPd | Solid | 0.810 (7) | Solid | 0.809 (6) |
| K733 | 5 | 1873 | 60 | AuPd | Solid/melt | 0.829 (6) | Solid | 0.815 (7) |
| K735 | 5 | 2073 | 30 | Pt | Melt | 0.828 (5) | n.i. | 0.828 (4) |
| K742 | 5 | 2273 | 10 | Pt | Melt | 0.822 (3) | Melt | 0.841 (8) |
| K745 | 15 | 1673 | 180 | AuPd | Solid | 0.826 (7) | | |
| K740 | 15 | 1873 | 60 | AuPd | Solid/melt | 0.804 (2) | Solid | 0.798 (2) |
| K749 | 15 | 2173 | 10 | Pt | Melt | 0.830 (6) | Melt | 0.841 (8) |

() Standard deviation of the last digit.
n.i. Not identified.

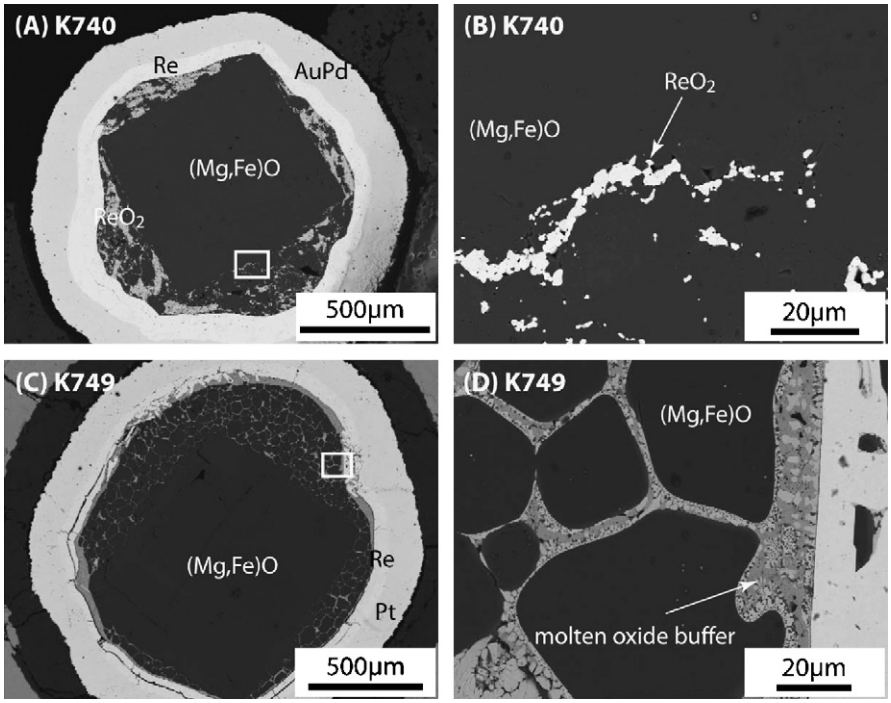


**Fig. 2.** Backscattered electron images of run products: (Mg,Fe)O single crystals annealed at 15 GPa, 1873 K with Re and solid $ReO_2$ (K740, A, B) and 15 GPa, 2173 K with Re and molten $ReO_2$ (K749, C, D). (B) and (C) are expansion of the rectangular areas in (A) and (C), respectively.

Geoinstitut. Synthetic $Mg_{0.8}Fe_{0.2}O$ single crystals were mounted in epoxy resin and polished down to a thickness of approximately 80 μm to optimize the absorber thickness, following Rancourt et al. (1993). A $^{57}Co$ radioactive source in a Rh matrix was used as a source of single-line γ-rays. The energy of the γ-rays were Doppler shifted with velocities ranging from +5 to −5 mm/s by moving the source relative to the sample in constant acceleration mode. The velocity scale of the spectrometer was calibrated relative to α-Fe foil. Ta foil with a 500 μm hole covered the sample to select the area to be measured. The γ-rays transmitted through the sample were measured using a detector coupled to a 512-channel multichannel analyser and the signal was folded to give a flat background.

## 3. Experimental results

### 3.1. High-pressure run products

The high-pressure annealing experiments of $Mg_{0.8}Fe_{0.2}O$ were conducted at 5 and 15 GPa at 1673–2273 K for 10–180 min (Table 1). Chemical equilibria in terms of $Fe^{3+}$ concentration should be achieved during the run durations if we assume that vacancy diffusion is the rate limiting process for $Fe^{3+}$ diffusion. The vacancy mobility of (Mg,Fe)O can be approximately estimated as

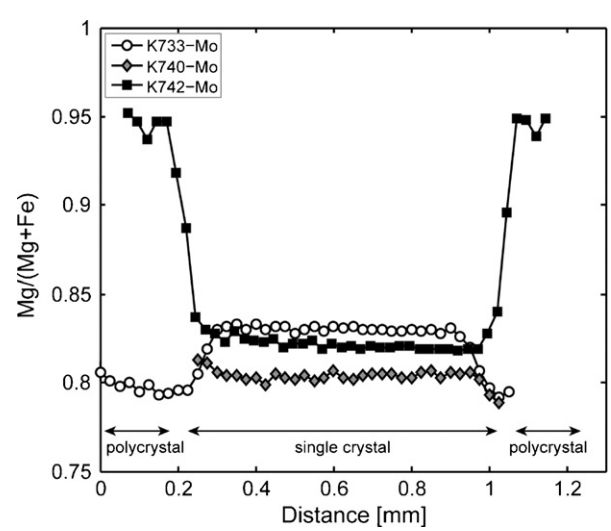


**Fig. 3.** Electron microprobe line profiles showing the chemical composition of run products (K733-Mo; K740-Mo; K742-Mo).

$6 \times 10^{-13}$ m$^2$/s at temperature of 1400 K and atmospheric pressure based on the Mg–Fe interdiffusion coefficient measured by Mackwell et al. (2005) and the $Fe^{3+}$ concentration measured by O'Neill et al. (2003). Activation energy of vacancy mobility was estimated as 220 kJ/mol (Sempolinski and Kingery, 1980). The activation volume of vacancy mobility is not well quantified, but is likely in the range from 1 to $2 \times 10^{-6}$ m$^3$/mol. (see more detailed discussion on the vacancy mobility and concentration in Section

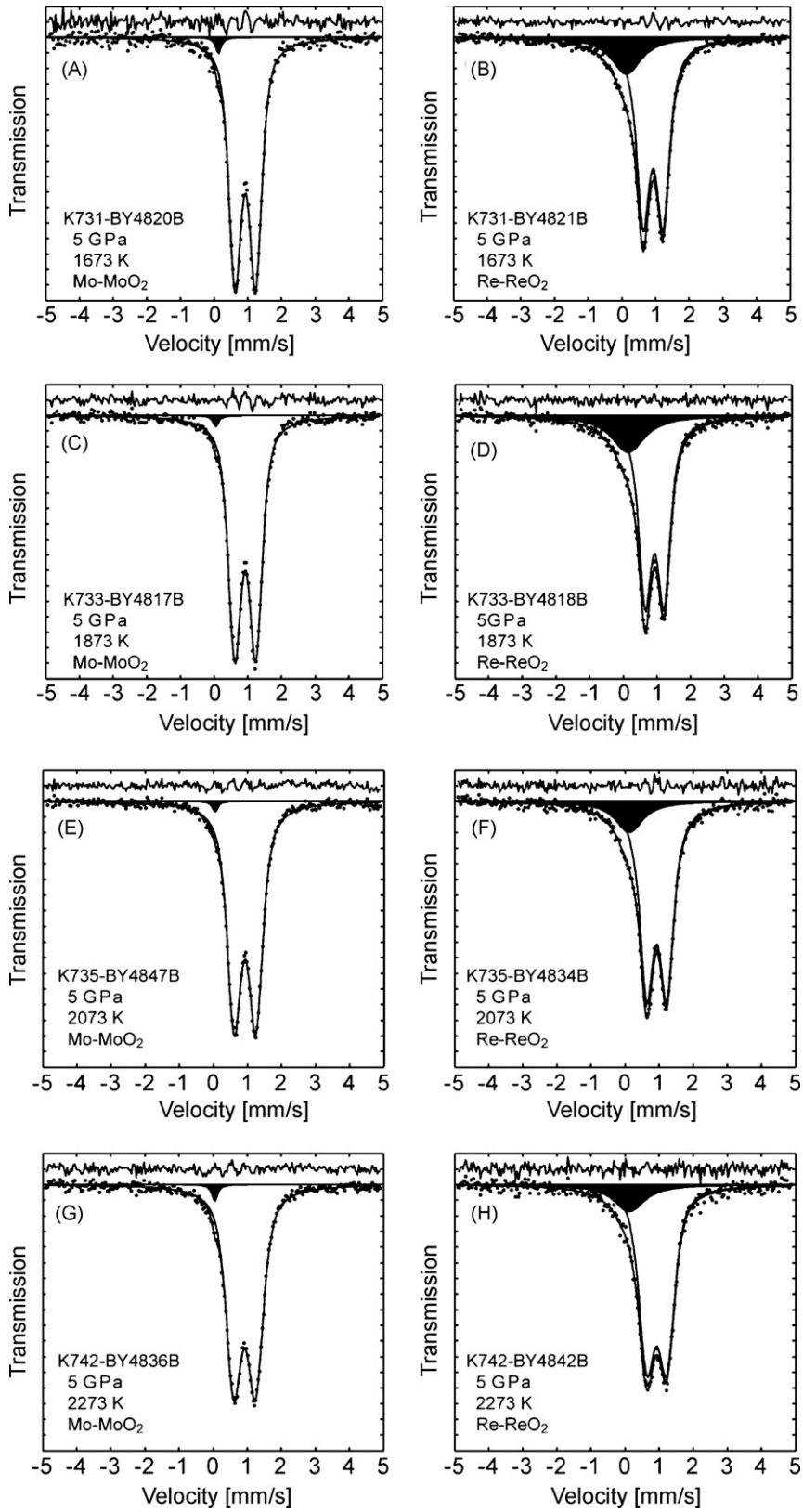


**Fig. 4.** Mössbauer spectra of $(Mg_{0.8}Fe_{0.2})O$ annealed at 1673–2273 K, 5 and 15 GPa with Mo–$MoO_2$ and Re–$ReO_2$. Experimental data is shown by dots, theoretical spectra by solid lines and the residual (experimental minus theoretical) is shown on the top. The absorption corresponding to $Fe^{3+}$ is shaded black.

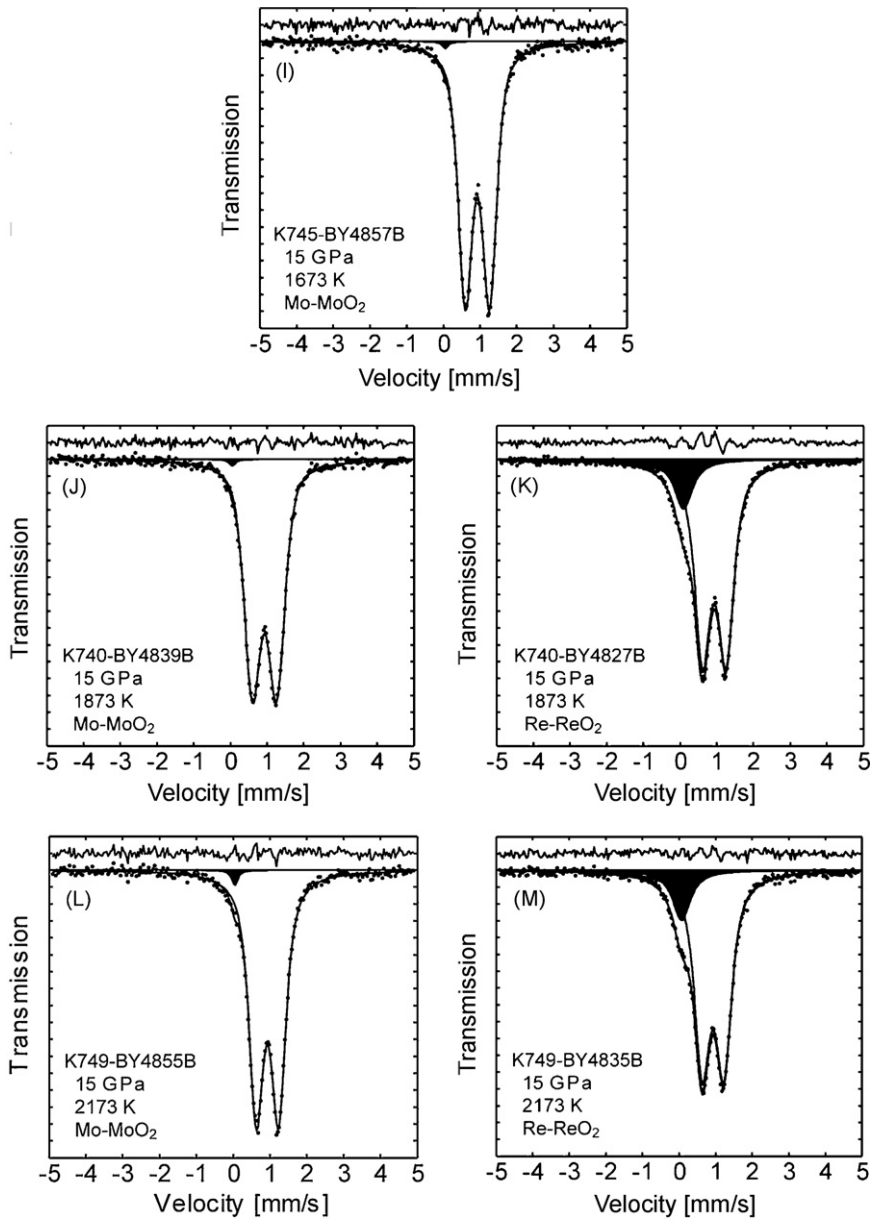


**Fig. 4.** (*Continued*).

4). Thus, the diffusion length scale of vacancy mobility during the experiments is more than the half of the thickness of the sample size (0.25 mm).

Synthetic $Mg_{0.8}Fe_{0.2}O$ single crystals recovered from annealing experiments were examined by scanning electron microscope. The presence of the oxygen fugacity buffer, either Re–$ReO_2$ or Mo–$MoO_2$, was confirmed for each sample (except $ReO_2$ of K735), indicating that oxygen fugacity was controlled by the metal and oxide buffers. The buffing oxide phases were round shaped crystals at temperatures below 1873 K, while they were quenched melt with dendritic textures at temperatures above 1873 K for $MoO_2$ and 2073 K for $ReO_2$ (Table 1, Fig. 2). The solid buffering oxides do not interconnect with each other, while molten buffering oxides wet the grain boundaries of (Mg,Fe)O (Fig. 2). Chemical compositions of single crystals were within an Mg# range from 80 to 84 (Table 1). During high-temperature experiments, the Mg# increased slightly towards the rim of the crystal due to the Fe loss into the melt (Fig. 3). The Mössbauer spectra were collected around the center of $Mg_{0.8}Fe_{0.2}O$ single crystals.

### 3.2. Mössbauer spectra

Each Mössbauer spectrum shows a dominant quadrupole doublet superimposed with a minor peak on the low-velocity shoulder of the major peak (Fig. 4). They are similar to the spectra reported in previous studies, where the major absorption peak corresponds to $Fe^{2+}$ and the minor peak to $Fe^{3+}$ (e.g., McCammon et al., 1998). No magnetic phases such as magnesioferrite were observed in any of the Mössbauer spectra. The hyperfine parameters were determined by fitting Mössbauer spectra using the commercially available computer software NORMOS. We found that the most stable fitting was obtained using one Voigt doublet (Rancourt and Ping, 1991) for the major peak and one Lorentzian singlet for the minor peak (Table 2). The distinct quadrupole splitting peaks observed for $Fe^{2+}$ absorption are well fitted by the Voigt doublet, which describes the total lineshape in terms of a Gaussian distribution sum of individual peaks with Lorentz lineshape. For the minor peak where two separate peaks could not be resolved only a Lorentzian singlet was used. More complicated fitting models such as a Voigt doublet were

**Table 2**
Hyperfine parameters derived from Mössbauer spectra.

| Run name | Temperature | $Fe^{2+}$ | | | | $Fe^{3+}$ | | Chi$\hat{2}$ | $Fe^{3+}/\sum Fe$ |
|---|---|---|---|---|---|---|---|---|---|
| | [K] | WID [mm/s] | ISO [mm/s] | QUA [mm/s] | STQ [mm/s] | WID [mm/s] | ISO [mm/s] | | [%] |
| Mo–$MoO_2$ at 5 GPa[a] | | | | | | | | | |
| K731-BY4820B | 1673 | 0.32 (2) | 0.926 (3) | 0.605 (3) | 0.096 (9) | 0.32 (2) | 0.12 (6) | 1.08 | 2.1 (4) |
| K733-BY4817B | 1873 | 0.32 (1) | 0.926 (1) | 0.621 (2) | 0.110 (5) | 0.32 (1) | 0.05 (2) | 1.48 | 2.4 (2) |
| K735-BY4847B | 2073 | 0.35 (2) | 0.929 (1) | 0.629 (2) | 0.112 (5) | 0.35 (1) | 0.06 (1) | 1.31 | 1.9 (2) |
| K742-BY4836B | 2273 | 0.38 (1) | 0.928 (2) | 0.631 (2) | 0.127 (6) | 0.38 (1) | 0.05 (2) | 1.17 | 3.0 (3) |
| Re–$ReO_2$ at 5 GPa[b] | | | | | | | | | |
| K731-BY4821B | 1673 | 0.44 (1) | 0.930 (2) | 0.590 (2) | 0.02 (2) | 1.07 (5) | 0.15 (2) | 1.12 | 20 (1) |
| K733-BY4818B | 1873 | 0.40 (2) | 0.931 (2) | 0.559 (3) | 0.04 (1) | 1.22 (9) | 0.15 (4) | 0.87 | 23 (2) |
| K735-BY4834B | 2073 | 0.44 (2) | 0.932 (2) | 0.587 (3) | 0.06 (1) | 0.99 (8) | 0.12 (3) | 1.12 | 16 (1) |
| K742-BY4842B | 2273 | 0.39 (3) | 0.925 (4) | 0.584 (5) | 0.12 (1) | 1.1 (1) | 0.08 (6) | 1.16 | 14 (2) |
| Mo–$MoO_2$ at 15 GPa[a] | | | | | | | | | |
| K745-BY4857B | 1673 | 0.31 (1) | 0.929 (1) | 0.656 (4) | 0.115 (6) | 0.31 (1) | 0.08 (4) | 1.14 | 0.8 (3) |
| K740-BY4839B | 1873 | 0.31 (1) | 0.933 (2) | 0.654 (2) | 0.148 (4) | 0.31 (1) | 0.08 (6) | 1.12 | 1.2 (3) |
| K749-BY4855B | 2173 | 0.37 (1) | 0.927 (1) | 0.605 (2) | 0.092 (6) | 0.37 (1) | 0.05 (2) | 0.98 | 2.3 (3) |
| Re–$ReO_2$ at 15 GPa[b] | | | | | | | | | |
| K740-BY4827B | 1873 | 0.42 (1) | 0.934 (1) | 0.641 (2) | 0.072 (5) | 0.59 (2) | 0.100 (6) | 2.75 | 14.0 (4) |
| K749-BY4835B | 2173 | 0.44 (1) | 0.930 (2) | 0.591 (2) | 0.065 (7) | 0.59 (2) | 0.075 (8) | 1.33 | 14.0 (6) |

WID: full Lorenzian line width at half maximum, ISO: isomer shift, QSD: quadrupole splitting, STQ: Gaussian standard deviation for quadrupole splitting distribution.
[a] Linewidth of $Fe^{3+}$ is constrained to be the same as the value for $Fe^{2+}$.
[b] Linewidth of $Fe^{3+}$ is not constrained to be the same as the value for $Fe^{2+}$.

attempted for the minor peak, but the residual after fitting was not significantly improved based on the chi-squared fitting test. The Lorentzian linewidths were fitted as variable parameters. The $Fe^{3+}$ linewidth was assumed to have the same value as the one for $Fe^{2+}$ in the case of low $Fe^{3+}$ concentration. The $Fe^{3+}/\sum Fe$ ratio was calculated based on the relative absorption areas for $Fe^{2+}$ and $Fe^{3+}$. We estimated the uncertainty based on the statistics of the fitting process and the uncertainty of the fitting model itself.

We particularly focus on the isomer shift within the set of determined hyperfine parameters since it is sensitive to valence state and the crystallographic position of iron (e.g., McCammon, 2004). The isomer shift relative to α-Fe determined for the $Fe^{2+}$ doublet varies no more than 0.01 mm/s over all spectra and agrees well with the typical value of 0.933 mm/s for $Fe^{2+}$ in the octahedral site (Waychunas, 1983). In contrast, the isomer shift of the $Fe^{3+}$ singlet varies systematically with the experimental conditions (Fig. 5). The isomer shift and concentration of $Fe^{3+}$ absorption are constrained by the asymmetry of the main doublet of $Fe^{2+}$, and are therefore relatively independent of the fitting model. The $Fe^{3+}$ isomer shifts are about 0.05 mm/s under reduced conditions buffered by Mo–$MoO_2$ except K731-BY4820B (5 GPa and 1673 K), whereas they are higher under oxidized conditions buffered by Re–$ReO_2$: around 0.13 mm/s at 5 GPa and 0.1–0.07 mm/s at 15 GPa. The pressure dependence of the isomer shift under oxidized conditions has not been discussed previously, but can be observed in Fig. 2 of McCammon et al. (1998). The observed values of the isomer shift indicate a variation of $Fe^{3+}$ site occupancy since it decreases with atomic distance to the first nearest neighbor: 0.24 mm/s for octahedral occupancy and 0.07 mm/s for tetrahedral occupancy (Waychunas, 1983). Thus,

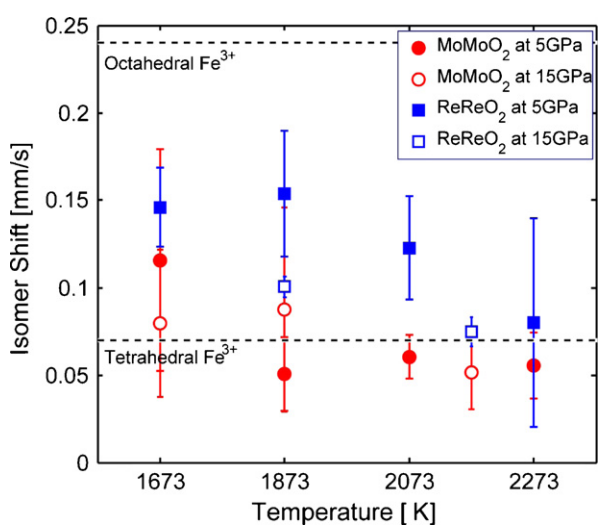


**Fig. 5.** Isomer shift of $Fe^{3+}$ as a function of annealing temperature. Mo–$MoO_2$ at 5 GPa (red solid circles) and at 15 GPa (red open circles); Re–$ReO_2$ in at 5 GPa (blue solid squares) and 15 GPa (blue open squares). The isomer shift relative to α-Fe in (Mg,Fe)O was determined as 0.24 mm/s and 0.07 mm/s for $Fe^{3+}$ in the octahedral and tetrahedral sites, respectively (Waychunas, 1983). (For interpretation of the references to color in this figure legend, the reader is referred to the web version of the article.).

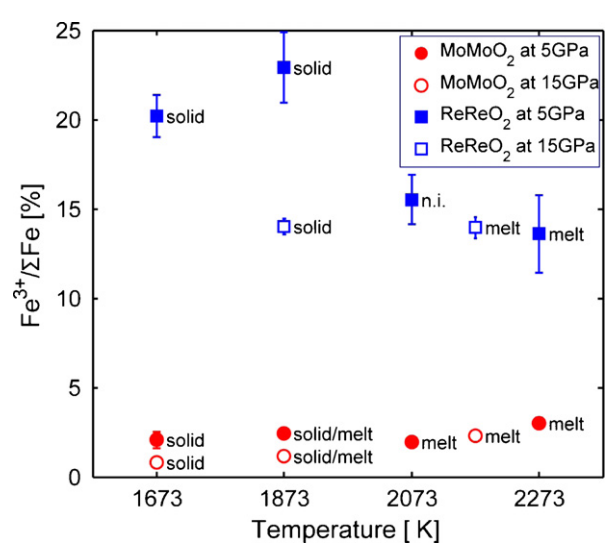


**Fig. 6.** $Fe^{3+}/\sum Fe$ as a function of annealing temperature. Mo–$MoO_2$ at 5 GPa (red solid circles) and at 15 GPa (red open circles); Re–$ReO_2$ at 5 GPa (blue solid squares) and 15 GPa (blue open squares). The data point labels indicate the conditions of the buffering oxide (n.i.: not identified). (For interpretation of the references to color in this figure legend, the reader is referred to the web version of the article.).

the low values of the isomer shift obtained under reduced conditions suggest tetrahedral occupancy of $Fe^{3+}$, while the high values under oxidized conditions suggest both tetrahedral and octahedral occupancies. The high isomer shift coincides with a broader linewidth up to around 1 mm/s. There are two possible explanations for the apparent broadening of the linewidth: large variability in the nuclear energy levels of $Fe^{3+}$ due to the multiple site occupations of $Fe^{3+}$, or large variations in quadrupole splitting.

Fig. 6 shows the relation between the $Fe^{3+}/\sum Fe$ ratio and the experimental conditions. $Fe^{3+}/\sum Fe$ increases with oxygen fugacity, and it decreases with pressure at low temperatures when the buffering oxide, either $MoO_2$ or $ReO_2$, is solid, while it remains almost constant at high temperatures when buffering oxide is quenched melt. $Fe^{3+}/\sum Fe$ at 5 GPa and 2073 K with the Re–$ReO_2$ buffer is lower than the trend extrapolated from low temperatures, which indicates the melting of the $ReO_2$ phase or a deficit of the $ReO_2$ phase. Quantitative discussion of the $Fe^{3+}$ concentration will be presented in the next section.

## 4. Discussion

### 4.1. A thermodynamic model

The Mössbauer spectra show that the $Fe^{3+}$ concentration and site occupation are influenced by temperature, pressure, and oxygen fugacity. Here, we present a simple thermodynamic model of $Fe^{3+}$ dissolution in (Mg,Fe)O to interpret the experimental data, especially at low defect concentration. We start by formulating the stoichiometric relations of point defects in (Mg,Fe)O. A general structural formula for (Mg,Fe)O solid solution can be described as

$$^{VI}[Mg, Fe^{2+}, Fe^{3+}, V]^{IV}[V, Fe^{3+}]_2[O] \tag{1}$$

where the superscripts VI and IV denote the octahedral and tetrahedral cation sites, respectively, and V indicates a cation vacancy. For simplicity we ignore other minor point defects such as O vacancies, $Mg^{2+}$ and $Fe^{2+}$ in the tetrahedral site, and trivalent cations such as $Al^{3+}$ and $Cr^{3+}$. The conservation of stoichiometry of the lattice sites gives the following two equations where we use the Kröger–Vink notation:

$$[Mg^{\times}_{VI}] + [Fe^{\times}_{VI}] + [Fe^{\cdot}_{VI}] + [V''_{VI}] = 1 \tag{2}$$

for the octahedral site, and

$$[V^{\times}_{IV}] + [Fe^{\cdots}_{IV}] = 1 \tag{3}$$

for the tetrahedral site, where the brackets denote the concentration in atomic fraction. The electrical neutrality condition is expressed as:

$$[Fe^{\cdot}_{VI}] + 6[Fe^{\cdots}_{IV}] = 2[V''_{VI}]. \tag{4}$$

Note that the tetrahedral site has a multiplicity of two per formula unit. This may be simplified if one of the positive defects is dominant: $[Fe^{\cdot}_{VI}] = 2[V''_{VI}]$ for the regime where octahedral $Fe^{3+}$ dominates or $3[Fe^{\cdots}_{IV}] = [V''_{VI}]$ for the regime where tetrahedral $Fe^{3+}$ dominates.

We now consider a chemical system consisting of (Mg,Fe)O and $O_2$ to describe the (Mg,Fe)O phase subjected to a change in the $Fe^{3+}/\sum Fe$ ratio through the interchange of an O atom with an external $O_2$ phase. The equilibrium between two phases is described by the following two relations:

$$2Fe^{\times}_{VI} + \tfrac{1}{2}O_2 = 2Fe^{\cdot}_{VI} + V''_{VI} + 2V^{\times}_{IV} + O^{\times}_{O} \tag{5}$$

for the formation of $Fe^{3+}$ in the octahedral site and

$$2Fe^{\times}_{VI} + \tfrac{1}{2}O_2 = 3V''_{VI} + 2Fe^{\cdots}_{IV} + O^{\times}_{O} \tag{6}$$

for $Fe^{3+}$ formation in the tetrahedral site. In the following discussion, we assume that (1) minor species ($Fe^{\cdot}_{VI}$, $Fe^{\cdots}_{IV}$, $V''_{VI}$) are completely disordered in the structure and their activities are proportional to their composition (Henry's Law), and (2) concentrations of major species ($Fe^{\times}_{VI}$, $V^{\times}_{IV}$, $O^{\times}_{O}$) do not change significantly. The law of mass action corresponding to reactions (5) and (6) gives

$$\frac{[Fe^{\cdot}_{VI}]^2[V''_{VI}]}{f_{O_2}^{1/2}} \propto \exp\left[-\frac{E^*_{R1} + PV^*_{R1}}{RT}\right], \tag{7}$$

$$\frac{[V''_{VI}]^3[Fe^{\cdots}_{IV}]^2}{f_{O_2}^{1/2}} \propto \exp\left[-\frac{E^*_{R2} + PV^*_{R2}}{RT}\right] \tag{8}$$

respectively, where $P$ is pressure, $T$ is temperature, $R$ is the gas constant, $E^*_{R1}$, $E^*_{R2}$ are the activation energies of reactions (i.e., enthalpy of the reaction at ambient pressure) (5) and (6), and $V^*_{R1}$, $V^*_{R2}$ are the volume change for the solid parts of the reactions (5) and (6). Henry's Law implies that the various point defects do not interact with each other, which is valid for solid solutions with sufficiently small defect concentrations. Substitution of the conservation equations for charge neutrality (Eq. (4)) into the mass action equations (Eqs. (7) and (8)) gives the equilibrium concentration of $Fe^{3+}$:

$$[Fe^{\cdot}_{VI}] \propto f_{O_2}^{1/6} \exp\left[-\frac{E^*_{R1} + PV^*_{R1}}{3RT}\right] \tag{9}$$

for the octahedral $Fe^{3+}$ dominant regime, and

$$[Fe^{\cdots}_{IV}] \propto f_{O_2}^{1/10} \exp\left[-\frac{E^*_{R2} + PV^*_{R2}}{5RT}\right] \tag{10}$$

for the tetrahedral $Fe^{3+}$ dominant regime. In either case, the concentration of vacancies is proportional to that of $Fe^{3+}$.

The model shows that the concentration of tetrahedral $Fe^{3+}$ is less sensitive to oxygen fugacity and pressure than for octahedral $Fe^{3+}$, since the oxygen fugacity exponent and activation volume for tetrahedral $Fe^{3+}$ are smaller than those of octahedral $Fe^{3+}$. This is due to the fact that the number of possible configurations during oxidation of (Mg,Fe)O is higher in the reaction involving tetrahedral $Fe^{3+}$ (Eq. (7)) than that involving octahedral $Fe^{3+}$ (Eq. (8)). Thus, the thermodynamic model described above suggests that (Mg,Fe)O accommodates tetrahedral $Fe^{3+}$ preferentially over octahedral $Fe^{3+}$ at high-pressure or low oxygen fugacity.

$Fe^{3+}$ concentration can also be written as

$$[Fe^{3+}] = A_C \exp\left[-\frac{E^*_C + PV^*_C}{RT}\right] \tag{11}$$

where $A_C$ is a constant, and $E^*_C$ and $V^*_C$ are the activation energy and activation volume, respectively, of $Fe^{3+}$ formation. Oxygen fugacity buffered by solid media follows an exponential relation:

$$f_{O_2} = A_F \exp\left[-\frac{E^*_F + PV^*_F}{RT}\right] \tag{12}$$

where $A_F$ is a constant, and $E^*_F$ and $V^*_F$ are the activation energy (i.e., enthalpy of reaction), and the volume change for the solid parts of the oxygen fugacity buffer, respectively. Thus, a comparison between Eqs. (9)–(12) gives

$$V^*_C = -\frac{V^*_F}{6} + \frac{V^*_{R1}}{3} \tag{13}$$

for the octahedral $Fe^{3+}$ dominant regime, and

$$V^*_C = -\frac{V^*_F}{10} + \frac{V^*_{R2}}{5} \tag{14}$$

for the tetrahedral $Fe^{3+}$ dominant regime. Table 3 summarizes the activation volume of the reactions. $V^*_F$ is estimated from the molar volumes of buffering materials (Nishihara et al., 2006), and $V^*_{R1}$, $V^*_{R2}$

**Table 3**
Summary of activation volumes.

| | Activation volume [$10^{-6}$ m$^3$/mol] |
|---|---|
| Oxygen fugacity buffer ($\Delta V_F^*$)[a] | |
| Mo–$MoO_2$ | 10.19 (2) |
| Re–$ReO_2$ | 9.94 (1) |
| Ni–NiO | 8.76 (7) |
| Fe–FeO | 9.90 (8) |
| $Fe^{3+}$ formation reaction ($\Delta V_R^*$)[b] | |
| $(Mg_{0.8}Fe_{0.2})O$ | 11.448 |

[a] Molar volumes are from Robie et al. (1978): $ReO_2$ 18.8(1), Re 8.860(4), $MoO_2$ 19.58(2), Mo 9.387(5), Ni 6.59(3), NiO 10.97(2), Fe 7.092(4), FeO 12.04(4), and MgO 11.248(4) in $10^{-6} \times m^3$/mol.
[b] Partial molar volumes of MgO and FeO in (Mg,Fe)O are from Frost et al. (2001): MgO 11.248, and FeO:12.250 in $10^{-6} \times m^3$/mol.

are estimated from the molar volume of (Mg,Fe)O, assuming that the presence of point defects does not change the size of the lattice site.

### 4.2. Pressure and temperature dependence of $Fe^{3+}$ concentration

Fig. 7 plots the $Fe^{3+}$ solubility in $(Mg_{0.8}Fe_{0.2})O$ obtained in this study as well as from previous studies (Bolfan-Casanova et al., 2002, 2006; Frost and Langenhorst, 2002; McCammon et al., 1998, 2004; McCammon, 1994) for oxygen fugacity buffered by metal and solid oxide buffers (A) and by metal and molten oxide buffers (B). In order to compare results from various studies with different compositions, Mg# is normalized to 80 assuming a homologous temperature scaling for the activation energy of $Fe^{3+}$ formation. The pressure dependence of $Fe^{3+}$ concentration under a solid buffer (Fig. 7A) suggests the presence of three different regimes depending on pressure and oxygen fugacity buffer: (1) low oxygen fugacity (Mo and solid $MoO_2$), (2) low pressure (<15 GPa) and high oxygen fugacity (Re and solid $ReO_2$), and (3) high-pressure (>15 GPa) and high oxygen fugacity (Re and solid $ReO_2$). We fitted each regime separately using Eq. (11) to provide a first order approximation of the dependence of $Fe^{3+}$ concentration on thermodynamic parameters (Table 4). In the first regime, fitting of our experimental results at reduced conditions (Mo and solid $MoO_2$) gives $V_C^*$ of $1.2(8) \times 10^{-6}$ m$^3$/mol, which agrees well with the model prediction for tetrahedral $Fe^{3+}$ under the Mo–$MoO_2$ buffer ($V_C^* = 1.23 \times 10^{-6}$ m$^3$/mol, from Eq. (14)). The extrapolation of the fitting result to room pressure and 1473 K yields slightly lower $Fe^{3+}$ concentrations than those found by McCammon (1994). In the second regime, fitting of our experimental results at oxidized conditions (Re and solid $ReO_2$) gives a slightly smaller value of $V_C^*$ ($0.7(3) \times 10^{-6}$ m$^3$/mol). Extrapolation of this result to higher pressure and low temperature yields higher $Fe^{3+}$ concentrations than the values determined by McCammon et al. (1998) and inferred from Bolfan-Casanova et al. (2002, 2006), indicating that the pressure dependence of $Fe^{3+}$ concentration increases with pressure. In the third regime, experimental data at high-pressure and oxidized conditions (Bolfan-Casanova et al., 2002, 2006; Frost and Langenhorst, 2002; McCammon et al., 1998, 2004) are insufficient to allow a confident regression of the activation volume. Thus, we assume $V_C^*$ to be $2.16 \times 10^{-6}$ m$^3$/mol, which is derived from the thermodynamic model for octahedral $Fe^{3+}$ under the Re–$ReO_2$ buffer (Eq. (13)). These observations on the change of the pressure dependence of $Fe^{3+}$ concentration agree qualitatively with the results of previous experiments performed at 1473 K and 5–25 GPa with Mg# 87 and 93 (Bolfan-Casanova et al., 2002, 2006). As shown in Fig. 7(B), in the cases where the buffering oxide is molten, $V_C^*$ is smaller than for the case of solid buffering material. This is attributable to the increase of molar volume of $MoO_2$ or $ReO_2$ during melting that affects the pressure dependence of oxygen fugacity for a given buffer.

**Table 4**
Fitting results for thermodynamic model.

| Oxygne fugacity buffer | $A_C$ | $E_C^*$ [kJ/mol] | $V_C^*$ [$10^{-6}$ m$^3$/mol] |
|---|---|---|---|
| This study | | | |
| Mo–$MoO_2$ (solid) | 0.02 (1) | 19 (7) | 1.2 (8) |
| Re–$ReO_2$ (solid) | 0.077 (8) | 6 (2) | 0.7 (3) |
| Mo–$MoO_2$ (melt) | 0.6 (1) | 85 (3) | 0.1 (5) |
| Re–$ReO_2$ (melt) | 0.007 (1) | −26 (4) | 0.1 (7) |
| Previous studies[a] | | | |
| Re–$ReO_2$ (solid) | 0.061 (2) | −16.1 (6) | 2.16[b] |

[a] Experimental data from Bolfan-Casanova et al. (2006, 2002), Frost and Langenhorst (2002); McCammon et al. (2004, 1998).
[b] Estimated from the model prediction for $Fe^{3+}$ in the octahedral site under the Re–$ReO_2$ buffer.

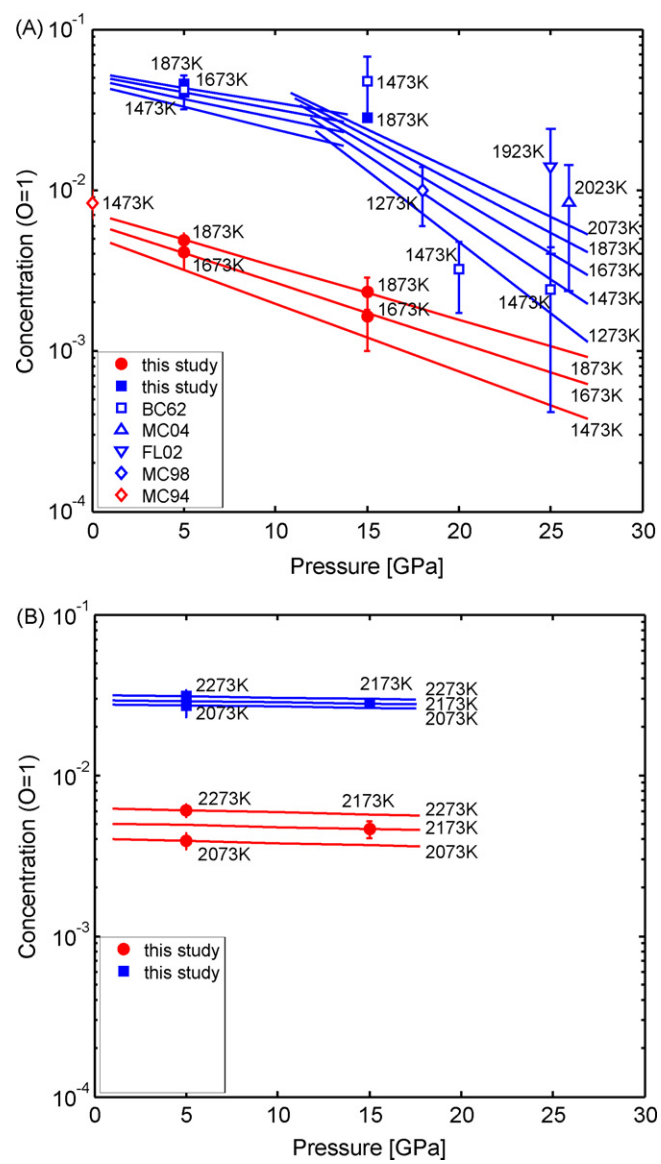


**Fig. 7.** $Fe^{3+}$ concentration in $(Mg_{0.8}Fe_{0.2})O$ as a function of annealing pressure. Color indicates the oxygen fugacity buffer: Mo–$MoO_2$ in red and Re–$ReO_2$ in blue. Solid lines are fitting results for solid buffering oxide (A) and for molten buffering oxide (B). Data are from this study, BC62: Bolfan-Casanova et al. (2006, 2002); MC04: McCammon et al. (2004); FL02: Frost and Langenhorst (2002); MC98: McCammon et al. (1998); MC94: McCammon (1994).

We infer that the observed three regimes of the pressure dependence of $Fe^{3+}$ concentration indicates a change of the dominant site occupation of $Fe^{3+}$: (1) unassociated $Fe^{3+}$ in the tetrahedral site, (2) unassociated $Fe^{3+}$ in the octahedral, and (3) defect clusters of $Fe^{3+}$ and cation vacancies, in the order of increasing oxygen fugacity and decreasing pressure. This inference is consistent with the observed isomer shift trend showing tetrahedral $Fe^{3+}$ under reduced conditions and both tetrahedral and octahedral $Fe^{3+}$ under oxidized conditions. The observed tetrahedral $Fe^{3+}$ under reduced conditions can be interpreted as unassociated defects based on the pressure dependence of $Fe^{3+}$ concentration. The proposed thermodynamic model supports the change from tetrahedral $Fe^{3+}$ to octahedral $Fe^{3+}$ with increasing oxygen fugacity or decreasing pressures. The mixed occupancy of $Fe^{3+}$ observed in Mössbauer spectra under oxidized conditions suggests the presence of tightly bound defect clusters of $Fe^{3+}$ both at octahedral and tetrahedral sites and cation vacancies (e.g., Gourdin and Kingery, 1979; Hazen and Jeanloz, 1984; Hilbrandt and Martin, 1998; Jacobsen et al., 2002), which is consistent with the fact that point defects interact with each other at high $Fe^{3+}$ concentrations.

The change of the dominant site occupancy of $Fe^{3+}$ with pressure is in reasonable agreement with the complicated dependence of $Fe^{3+}$ concentration on oxygen fugacity observed by Speidel (1967). They performed a thermogravimetric study over a broad range of oxygen fugacity from the stability field of metallic Fe to magnesioferrite. We re-analyzed their data in high Mg# (89 and 75) and found that the oxygen fugacity dependence of $Fe^{3+}$ concentration systematically changes with oxygen fugacity: a weak dependence of oxygen fugacity at reduced conditions (fugacity exponent ($n$) of ~1/10), a gradual increase in oxygen fugacity dependence at intermediate conditions ($n$ up to ~1/4), and a weak dependence at oxidized conditions ($n < 1/10$). The change of fugacity exponent at low to intermediate fugacity agrees well with model predictions for the unassociated point defects: the fugacity exponent increases with oxygen fugacity from $n = 1/10$ for tetrahedral $Fe^{3+}$ (Eq. (10)) to $n = 1/6$ for octahedral $Fe^{3+}$ (Eq. (9)).

Independent evidence for the change of $Fe^{3+}$ site occupation comes from measurements of transport properties: electrical conductivity and Mg–Fe interdiffusivity. Firstly, electrical charge transfer in (Mg,Fe)O at low temperature (<1000 K) occurs by electron hopping between $Fe^{2+}$ and $Fe^{3+}$ and by ionic diffusion at high temperature (>1000 K) (Dobson et al., 1997). Thus, a linear correlation between electrical conductivity and $Fe^{3+}$ content is expected in the case of $Fe^{2+} \gg Fe^{3+}$. Measurements of electrical conductivity of (Mg,Fe)O with a Mg# range from 99 to 80 at 1073–1273 K show that the power dependence of conductivity with oxygen fugacity ranges from 1/10 to 1/3 depending on Mg# and temperature (Iyengar and Alcock, 1970). Based on the thermodynamic consideration, a weak dependence ($n = 1/8$–$1/10$) observed at low Fe content (Mg# > 95) indicates the presence of $Fe^{3+}$ in the tetrahedral site, whereas a strong dependence ($n = 1/6$–$1/4$) at high Fe content (Mg# < 95) indicates $Fe^{3+}$ in the octahedral site or a composite of simple defect associates such as $Fe^{3+}$-vacancy dimer or trimer (e.g., Gourdin and Kingery, 1979). Secondly, Mg–Fe interdiffusion in (Mg,Fe)O can be interpreted in terms of vacancy mechanisms (e.g., Mackwell et al., 2005), where the pressure dependence of Mg–Fe interdiffusion ($V_D^*$) includes the pressure dependence of vacancy concentration ($V_C^*$) as well as vacancy mobility ($V_M^*$). $V_D^*$ was determined by two recent studies as $1.8(10) \times 10^{-6}$ $m^3$/mol under the Re–$ReO_2$ buffer at 1573–1973 K and 7–35 GPa (Yamazaki and Irifune, 2003), and $3.3(1) \times 10^{-6}$ $m^3$/mol under the Ni–NiO buffer at 1673–1873 K and 8–23 GPa (Holzapfel et al., 2003). Based on our observations of pressure dependence of $Fe^{3+}$ concentration, this discrepancy is likely due to the oxygen fugacity dependence of $V_C^*$ : low $V_C^*$ at high oxygen fugacity (Re–$ReO_2$) due to complex defect clusters and high $V_C^*$ at intermediate oxygen fugacity (Ni–NiO) due to $Fe^{3+}$ in the octahedral site.

### 4.3. Implications for the lower mantle

On the basis of experimental results and the thermodynamic considerations described above, we conclude that tetrahedral $Fe^{3+}$ is stabilized relative to octahedral $Fe^{3+}$ at high-pressure and low oxygen fugacity due to the influence of the configurational entropy. The oxygen fugacity in the lower mantle is estimated as 1.4 log–bar units below Fe–$Fe_{1-\delta}O$ (Frost and McCammon, 2008) due to the presence of metallic Fe (Frost et al., 2004), which is even lower than the experimental conditions. We thus consider it plausible that (Mg,Fe)O accommodates $Fe^{3+}$ in the tetrahedral site down to the lower mantle. Fig. 8 illustrates our estimates of $Fe^{3+}$ concentration under the oxygen fugacity of the lower mantle compared with the $H^+$ solubility determined under water-saturated conditions by Bolfan-Casanova et al. (2002); Murakami et al. (2002). We calculated the $Fe^{3+}$ concentration in the lower mantle by extrapolating our results under reduced conditions assuming a Mg# of 80 and the fugacity exponent of 1/10 (Eq. (10)). $Fe^{3+}$ concentration was estimated as ~650 ppm ($Fe^{3+}$/O) at 1873 K and 25 GPa at the top of the lower mantle. As shown in Fig. 8, two recent studies yield markedly different results on $H^+$ (or $H_2O$) solubility in (Mg,Fe)O (see Hirschmann, 2006 for a review). Bolfan-Casanova et al. (2002) obtained the solubility of $H^+$ in $(Mg_{0.93}Fe_{0.07})O$ as ~100 ppm H/O at 1473 K and 25 GPa, while Murakami et al. (2002) determined the $H^+$ solubility in $(Mg_{0.92}Fe_{0.08})O$ as ~10,000 ppm H/O at 1923 K and 25.5 GPa. Thus, the exact conditions of the solubility crossover between $Fe^{3+}$ and $H^+$ are poorly constrained due to the large discrepancy in $H^+$ solubility. The spin crossover transition of Fe at high-pressure (starting around 40 GPa, Tsuchiya et al., 2006; Lin et al., 2007) potentially changes the behavior of point defects by decreasing the effective ionic radius of iron.

Recently, Demouchy et al. (2007) obtained a factor of four enhancement of Mg–Fe interdiffusivity in (Mg,Fe)O under water-saturated conditions at 300 MPa and 1273–1423 K, as compared with experiments under anhydrous conditions by Mackwell et al. (2005). They attributed the enhanced diffusivity to the increased defect concentration by the dissolution of water. However, over the most of the Mg# range that they studied, cation vacancies charge balanced by $Fe^{3+}$ are significantly more abundant than those charge balanced by $H^+$. It is thus not yet clear how $H^+$ enhances

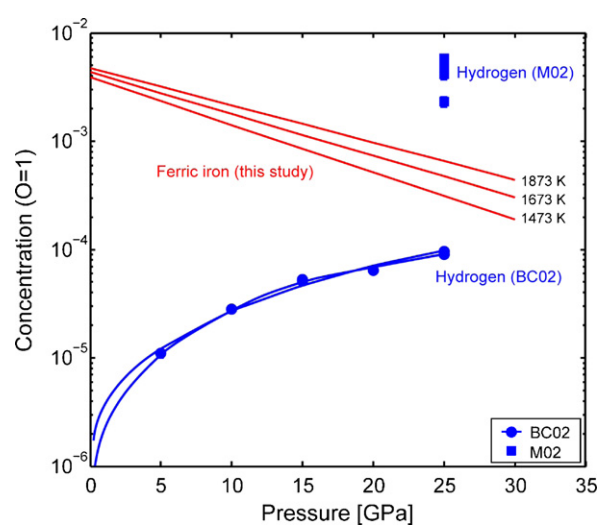


**Fig. 8.** Solubility of $Fe^{3+}$ and $H^+$ in (Mg,Fe)O as a function of pressure. $Fe^{3+}$ solubility in (Mg,Fe)O decreases with pressure, while the $H^+$ solubility increases. Data are from this study, BC02: Bolfan-Casanova et al. (2002); M02: Murakami et al. (2002).

interdiffusion under the $Fe^{3+}$-dominant regime. More importantly, extrapolation of their results to lower mantle conditions may substantially underestimate the influence of water in the lower mantle where $H^+$ concentration may dominate over $Fe^{3+}$ solubility. Further high-pressure studies are needed to determine the relative contributions of oxygen fugacity ($Fe^{3+}$ content) and water fugacity ($H^+$ content) on transport properties in the lower mantle.

## Acknowledgements

This work was supported by the National Science Foundation under grant no. EAR-0809330. We are grateful to James Eckert and Zhenting Jiang for their assistance in electron microprobe analysis; and to Takaaki Kawazoe, Zhicheng Jing, and Mainak Mookherjee for their assistance with the multi-anvil experiments and to Micaela Longo for discussion on Mössbauer spectroscopy. We wish to thank Yu Nishihara and Jim Van Orman for constructive reviews.

## References

Bolfan-Casanova, N., Mackwell, S., Keppler, H., McCammon, C., Rubie, D.C., 2002. Pressure dependence of H solubility in magnesiowüstite up to 25 GPa: implications for the storage of water in the Earth's lower mantle. Geophys. Res. Lett. 29 (10), 1029–1032.

Bolfan-Casanova, N., McCammon, C., Mackwell, S., 2006. Water in transition zone and lower mantle minerals. In: Jacobsen, S.D., van der Lee, S. (Eds.). Earth's deep water cycle. Am. Geophys. Union, Geophys. Monogr. Ser. 168, 57–68.

Demouchy, S., Mackwell, S.J., Kohlstedt, D.L., 2007. Influence of hydrogen on Fe–Mg interdiffusion in (Mg,Fe)O and implications for Earth's lower mantle. Contrib. Mineral. Petrol., doi:10.1007/s00410-007-0193-9.

Dobson, D.P., Richmond, N.C., Brodholt, J.P., 1997. A high-temperature electrical conduction mechanism in the lower mantle phase $(Mg,Fe)_{1-x}O$. Science 275 (5307), 1779–1781.

Frost, D.J., Langenhorst, F., 2002. The effect of $Al_2O_3$ on Fe–Mg partitioning between magnesiowüstite and magnesium silicate perovskite. Earth Planet. Sci. Lett. 199 (1–2), 227–241.

Frost, D.J., Langenhorst, F., van Aken, P.A., 2001. Fe–Mg partitioning between ringwoodite and magnesiowüstite and the effect of pressure, temperature and oxygen fugacity. Phys. Chem. Miner. 28, 455–470.

Frost, D.J., Liebske, C., Langenhorst, F., McCammon, C.A., Trønnes, R.G., Rubie, D.C., 2004. Experimental evidence for the existence of iron-rich metal in the Earth's lower mantle. Nature 428 (6981), 409–412.

Frost, D.J., McCammon, C.A., 2008. The redox state of Earth's mantle. Ann. Rev. Earth Planet. Sci. 36, 389–420.

Gourdin, W.H., Kingery, W.D., 1979. The defect structure of MgO containing trivalent cation solutes: shell model calculations. J. Mater. Sci. 14, 2053–2073.

Hazen, R.M., Jeanloz, R., 1984. Wustite ($Fe_{1-X}O$): a review of its defect structure and physical properties. Rev. Geophys. 22 (1), 37–46.

Hilbrandt, N., Martin, M., 1998. High temperature point defect equilibria in iron-doped MgO: an *in situ* Fe–K XAFS study on the valance and site distribution of iron in $(Mg_{1-x}Fe_x)O$. Ber. Bunsen. Phys. Chem. 102, 1747–1759.

Hirose, K., 2002. Phase transitions in pyrolitic mantle around 670-km depth: implications for upwelling of plumes from the lower mantle. J. Geophys. Res. 107 (B4), 2078, doi:10.1029/2001JB000597.

Hirsch, L.M., Shankland, T.J., 1991. Determination of defect equilibria in minerals. J. Geophys. Res. 96 (B1), 377–384.

Hirschmann, M.M., 2006. Water, melting, and the deep Earth $H_2O$ cycle. Ann. Rev. Earth Planet. Sci. 34, 629–653.

Holzapfel, C., Rubie, D.C., Mackwell, S., Frost, D.J., 2003. Effect of pressure on Fe–Mg interdiffusion in $(Fe_xMg_{1-x})O$, ferropericlase. Phys. Earth Planet. Int. 139 (1–2), 21–34.

Iyengar, G.N.K., Alcock, C.B., 1970. A study of semiconduction in dilute Magnesio–Wüstite. Philos. Mag. 21 (170), 293–304.

Jacobsen, S.D., Reichmann, H.J., Spetzler, H.A., Mackwell, S.J., Smyth, J.R., Angel, R.J., McCammon, C.A., 2002. Structure and elasticity of single-crystal (Mg,Fe)O and a new method of generating shear waves for gigahertz ultrasonic interferometry. J. Geophys. Res. 107 (B2), doi:10.1029/2001JB000490.

Katsura, T., Kimura, S., 1965. Equilibria in system $FeO–Fe_2O_3–MgO$ at 1160 °C. Bull. Chem. Soc. Jpn. 38 (10), 1664–1670.

Kelbert, A., Schultz, A., Egbert, G., 2009. Spatial variability of mantle transition zone water content: evidence from global electromagnetic induction data. Nature 460, doi:10.1038/nature08257.

Lawrence, J.F., Wysession, M.E., 2006. Seismic evidence for subduction-transported water in the lower mantle. In: Jacobsen, S.D., van der Lee, S. (Eds.). Earth's Deep Water Cycle. Am. Geophys. Union, Geophys. Monogr. Ser., 168, 251–261.

Lin, J.F., Vankó, G., Jacobsen, S.D., Iota, V., Struzhkin, V.V., Prakapenka, V.B., Kuznetsov, A., Yoo, C.H., 2007. Spin transition zone in earth's lower mantle. Science 317 (5845), 1740–1743.

Mackwell, S., Bystricky, M., Sproni, C., 2005. Fe–Mg interdiffusion in (Mg,Fe)O. Phys. Chem. Miner. 32 (5–6), 418–425.

McCammon, C., Peyronneau, J., Poirier, J.P., 1998. Low ferric iron content of (Mg,Fe)O at high pressures and temperatures. Geophys. Res. Lett. 25 (10), 1589–1592.

McCammon, C.A., 1994. Mössbauer spectroscopy of quenched high-pressure phases: investigating the Earths interior. Hyper. Int. 90 (1–4), 89–105.

McCammon, C.A., 2004. Mössbauer spectroscopy: applications. In: Beran, A. Libowitzky, E. (Eds.). Spectroscopic Methods in Mineralogy. Eur. Mineral. Union, Notes in Mineralogy, 6, 369–398.

McCammon, C.A., Lauterbach, S., Seifert, F., Langenhorst, F., van Aken, P.A., 2004. Iron oxidation state in lower mantle mineral assemblages I. Empirical relations derived from high-pressure experiments. Earth Planet. Sci. Lett. 222 (2), 435–449.

Murakami, M., Hirose, K., Yurimoto, H., Nakashima, S., Takafuji, N., 2002. Water in Earth's lower mantle. Science 295, 1885, doi:10.1126/science.1065998.

Nishihara, Y., Shinmei, T., Karato, S., 2006. Grain-growth kinetics in wadsleyite: effects of chemical environment. Phys. Earth Planet. Int. 154 (1), 30–43.

Ohta, K., Hirose, K., Onoda, S., Shimizu, K., 2007. The effect of iron spin transition on electrical conductivity of (Mg,Fe)O magnesiowüstite. Proc. Jpn. Acad., Ser. B 83, 97–100, doi:10.2183/pjab.83.97.

O'Neill, H.S.C., Powneeby, M.I., McCammon, C.A., 2003. The magnesiowüstite: iron equilibrium and its implications for the activity-composition relations of $(Mg,Fe)_2SiO_4$ olivine solid solutions. Contrib. Mineral. Petrol. 146, 308–325, doi:10.1007/s00410-003-0496-4.

Poirier, J.P., Peyronneau, J., Madon, M., Guyot, F., Revcolevschi, A., 1986. Eutectoid phase transformation of olivine and spinel into perovskite and rock salt Structures. Nature 321 (6070), 603–605.

Rancourt, D.G., Mcdonald, A.M., Lalonde, A.E., Ping, J.Y., 1993. Mössbauer absorber thicknesses for accurate site populations in Fe-bearing minerals. Am. Mineral. 78 (1–2), 1–7.

Rancourt, D.G., Ping, J.Y., 1991. Voigt-based methods for arbitrary-shape static hyperfine parameter distributions in Mössbauer spectroscopy. Nucl. Instrum. Methods Phys. Res. B58, 85–97.

Robie, R.A., Hemingway, B.S., Fisher, J.R., 1978. Thermodynamic properties of minerals and related substances at 298.15 K and 1 bar ($10^5$ pascals) pressure and at higher temperatures. U.S. Government Printing Office, U.S. Geol. Survey Bull., 1452, Washington, 456 pp.

Sempolinski, D.R., Kingery, W.D., 1980. Ionic conductivity and magnesium vacancy mobility in magnesium oxide. J. Am. Ceram. Soc. 63 (11–12), 664–669.

Speidel, D.H., 1967. Phase equilibria in the system $MgO–FeO–Fe_2O_3$: the 1300 °C isothermal section and extrapolations to other temperatures. J. Am. Ceram. Soc. 50 (5), 243–248.

Tsuchiya, T., Wentzcovitch, R.M., da Silva, C.R.S., de Gironcoli, S., 2006. Spin transition in magnesiowüstite in Earth's lower mantle. Phys. Rev. Lett. 96, 198501, doi:10.1103/PhysRevLett.96.198501.

Van Orman, J.A., Li, C., Crispin, K.L., 2009. Aluminum diffusion and Al-vacancy association in periclase. Phys. Earth Planet. Int. 172 (1–2), 34–42.

Waychunas, G.A., 1983. Mössbauer, EXAFS, and X-ray-diffraction study of $Fe^{3+}$ clusters in MgO: Fe and magnesiowüstite $(Mg,Fe)_{1-X}O$-evidence for specific cluster geometries. J. Mater. Sci. 18 (1), 195–207.

Wood, B.J., Nell, J., 1991. High-temperature electrical conductivity of the lower-mantle phase (Mg,Fe)O. Nature 351 (6324), 309–311.

Xu, Y.S., McCammon, C., 2002. Evidence for ionic conductivity in lower mantle $(Mg,Fe)(Si,Al)O_3$ perovskite. J. Geophys. Res. 107 (B10), 2251, doi:10.1029/2001JB000677.

Yamazaki, D., Irifune, T., 2003. Fe-Mg interdiffusion in magnesiowüstite up to 35 GPa. Earth Planet. Sci. Lett. 216 (3), 301–311.

Yamazaki, D., Karato, S., 2001. Some mineral physics constraints on the rheology and geothermal structure of Earth's lower mantle. Am. Mineral. 86 (4), 385–391.